

## Effects of Alkali Metal and Ammonium Cation Templates on Nanofibrous Cryptomelane-type Manganese Oxide Octahedral Molecular Sieves (OMS-2)

Jia Liu,<sup>†,‡</sup> Vinit Makwana,<sup>‡</sup> Jun Cai,<sup>‡</sup> Steven L. Suib,<sup>\*,†,‡,§</sup> and Mark Aindow<sup>†,||</sup>

*Institute of Materials Science, University of Connecticut, Unit 3136, Storrs, Connecticut 06269-3136, Department of Chemistry, University of Connecticut, Unit 3060, Storrs, Connecticut 06269-3060, Department of Chemical Engineering, University of Connecticut, Unit 3222, Storrs, Connecticut 06269-3222, and Department of Metallurgy and Materials Engineering, University of Connecticut, Unit 3136, Storrs, Connecticut 06269-3136*

*Received: January 16, 2003; In Final Form: April 23, 2003*

Four alkali cations ( $\text{Li}^+$ ,  $\text{Na}^+$ ,  $\text{K}^+$ , and  $\text{Rb}^+$ ) and ammonium ( $\text{NH}_4^+$ ), have been successfully used as templates for the synthesis of cryptomelane-type manganese oxide octahedral molecular sieves (A–OMS-2, A = the template cation). H–OMS-2 material has been prepared by the calcination of  $\text{NH}_4$ –OMS-2. These A–OMS-2 materials have been characterized by X-ray diffraction, transmission electron microscopy, high-resolution scanning electron microscopy, thermogravimetric analysis, temperature-programmed desorption, inductively coupled plasma analysis, and BET surface area pore size distribution measurements. Catalytic evaluation of these A–OMS-2 materials has been done with the aerobic oxidation of cyclohexanol to cyclohexanone. All of these A–OMS-2 materials have cryptomelane tunnel structures with different degrees of crystallinity and nanofibrous morphology. The nature of the cation templates affects the formation and microstructures of the A–OMS-2 materials. The physical and chemical properties, such as the thermal stability, chemical composition, and average oxidation state of manganese, greatly depend on the nature of cations and amount of tunnel water. Catalytic activities of these A–OMS-2 materials are related to their surface areas.

### Introduction

Cryptomelane-type manganese oxide octahedral molecular sieves (OMS-2) are microporous materials. The frameworks of OMS-2 materials are made of edge-shared  $\text{MnO}_6$  octahedra that form  $2 \times 2$  tunnels with a pore size of about 4.6 Å. Manganese in OMS-2 are  $\text{Mn}^{4+}$  and  $\text{Mn}^{3+}$  located in octahedral sites. In the tunnels, cations (e.g.,  $\text{K}^+$ ) reside with a small amount of water to stabilize the tunnel structure. Potassium in the tunnel can be partly ion-exchanged with other cations.<sup>1–5</sup> Due to the unique tunnel structure of OMS-2 and mixed-valent manganese, OMS-2 materials have potential applications as ion-exchange materials, battery materials, chemical sensors, electromagnetic materials, and catalysts.<sup>5,6</sup> Recent studies have been reported in detail on the catalytic applications of OMS-2 materials in several reactions, such as low-temperature carbon monoxide oxidation,<sup>7</sup> 2-propanol decomposition,<sup>8</sup> and aerobic oxidation of benzyl alcohol.<sup>9</sup> Syntheses and properties of bulk OMS-2 materials have been intensively studied in the past decade. Various methods have been used to prepare cryptomelane materials, such as thermal and hydrothermal methods to synthesize cryptomelane bulk materials from birnessites,<sup>10–13</sup> reflux methods to prepare cryptomelane from the oxidation of  $\text{Mn}^{2+}$  in acidic media,<sup>14–18</sup> and sol–gel methods to make cryptomelane from the reaction between  $\text{KMnO}_4$  and fumaric acid.<sup>19,20</sup> The products from these syntheses are potassium-type bulk materials (K–OMS-2). The morphologies of these OMS-2

materials have either platelike or needlelike shapes with large particle sizes.

To achieve better electronic and catalytic performance of OMS-2, metal cations have been incorporated into OMS-2 materials to alter structures and properties of OMS-2 materials by substituting for potassium or manganese ions, because physical and chemical properties of OMS-2 materials can be greatly influenced by doping cations of different types, amounts, and doping locations.<sup>4,5</sup> Substitution pathways reported include solid-state conversions from metal-doped birnessite,<sup>11–13</sup> aqueous a priori incorporation using redox reactions of  $\text{MnO}_4^{4-}$ – $\text{Mn}^{2+}$  and metal dopant cations,<sup>15,16</sup> and ion-exchange reactions to substitute partially for potassium ions in the tunnel sites with metal dopants in OMS-2 materials.<sup>3,18</sup>

Doping products of OMS-2 in solid-state conversions easily leads to the formation of hausmannite or bixbyites, except for a few transition metal ions doped into the frameworks of OMS-2 materials within certain doping capacities.<sup>12,13</sup> In aqueous priori incorporation methods, pyrolusite or nsutite can be easily formed as a byproduct due to the strong acidic media used in the syntheses. The doping capacities of metal ions, including main-group and transition-group cations, were limited because potassium was an important factor for growth and stability of OMS-2 structures.<sup>15,16</sup> Ion-exchange reactions can only be used to substitute small amounts of potassium cations in the tunnel with other metal ions.<sup>3,15c</sup> For better ion-exchange capacities, special treatments were needed, such as acid extraction and an extended reaction time from days to a week.<sup>18</sup>

For a long time, potassium ions have been taken as the ideal cation templates to form and stabilize the  $2 \times 2$  tunnel structure in synthetic cryptomelane materials, because the dimensions of the tunnel sizes of OMS materials were believed to be controlled

\* Author to whom correspondence should be addressed. E-mail: Suib@uconnvm.uconn.edu.

<sup>†</sup> Institute of Materials Science.

<sup>‡</sup> Department of Chemistry.

<sup>§</sup> Department of Chemical Engineering.

<sup>||</sup> Department of Metallurgy and Materials Engineering.

directly by the sizes of the templates used.<sup>22–24</sup> The study on the use of metal cations other than  $K^+$  as tunnel templates to synthesize OMS-2 materials has been left as an open field for OMS materials. The only extensive research that has been done in this field was reported recently.<sup>25</sup> Polyphosphate species were used in a condensed solution to assist sodium cations in the preparation of Na-OMS-2 materials. Weeks were needed to prepare the Na-OMS-2 materials by this method.

In this paper, we report for the first time systematically using other alkali metal cations (e.g.,  $Li^+$ ,  $Na^+$ ,  $Rb^+$ ) and  $NH_4^+$  cations, besides  $K^+$ , as templates to successfully synthesize  $2 \times 2$  tunnel structures (A-OMS-2, A = Li, Na, K, Rb, or  $NH_4$ ). Some of the A-OMS-2 materials, such as Li-OMS-2 and Rb-OMS-2, have not been reported before. The synthesis procedures are simple, and the formation of A-OMS-2 (A = Li, K, Rb, or  $NH_4$ ) materials can be completed in a few hours. Preparation of Na-OMS-2 was shortened to 3 days. These A-OMS-2 materials not only have a pure crystalline phase of cryptomelane, but also have unique long nanofibrous morphologies that had not been observed in conventional OMS-2 materials. Chemical and physical properties of A-OMS-2 materials have been investigated. Effects of different types of alkali metal and ammonium cation templates on the formation of tunnel structures and properties of the resulting A-MS-2 materials have also been studied. H-OMS-2 materials have been prepared by the calcination of  $NH_4$ -OMS-2 materials. All of these A-OMS-2 materials have been evaluated for their catalytic activities with an aerobic oxidation reaction of cyclohexanol to cyclohexanone. The conversions of A-OMS-2 materials have been compared with those of conventional K-OMS-2 materials.

## Experimental Section

**1. Synthesis of A-OMS-2 Nanofibrous Materials.** Nanofibrous A-OMS-2 materials were prepared by a method described in a previous paper.<sup>26</sup> A-OL-1 precursors were prepared from a tetraethylammonium (TEA) manganese oxide gel ( $TEAMnO_x$ ).<sup>27</sup> A 50 mL quantity of  $TEAMnO_x$  gel was added to a solution of 200 mL of 1 M  $ANO_3$  with stirring. Black precipitates were formed immediately. This suspension solution was subjected to ultrasonic vibration for 10 min and was stirred for an additional 1 h. The precipitates were washed 3–4 times by centrifugation and were sealed into a Teflon-lined autoclave. To study the effects of alkali cations on the transformation process, the autoclaved A-OL-1 samples were hydrothermally heated at 120–200 °C for a few hours to a few days. The resulting solids were washed three times with distilled deionized water (DDW) and dried at 85 °C in air. To prepare H-OMS-2, the resultant  $NH_4$ -OMS-2 solids were first ground. The black powders were then calcined at 350–380 °C for 8 h.

**2. Characterization.** *2.1. Structural Studies by XRD and TEM.* XRD data were collected on a Scintag XDS 2000 diffractometer with Cu  $K\alpha$  radiation. Washed samples were placed on glass slides when they were still wet and dried at room temperature. Selected area electron diffraction (SAED) data were obtained using a Philips EM420 transmission electron microscope (TEM) at 100 kV. A drop of A-OMS-2 nanofibrous suspension diluted in acetone was placed onto a holey carbon film supported by a 3-mm copper grid, and the solvent was allowed to evaporate. TEM bright field (BF) images of A-OMS-2 materials were also acquired. Some poorly crystalline materials were examined using a JEOL 2010 Fas TEM at 200 kV.

*2.2. Morphology.* The morphologies of A-OMS-2 materials were investigated using a Zeiss DSM 982 Gemini field emission

scanning electron microscope (FESEM) with a Schottky emitter. The sample suspension in acetone was dispersed on AuPd-coated silicon chips that had been mounted onto the stainless steel sample holders using silver conductive paint.

*2.3. Elemental Analyses and Average Oxidation State Determination.* The quantitative analyses of cation templates and manganese ions in the A-OMS-2 materials were carried out with a Perkin-Elmer model 140 ICP-AES instrument. The average oxidation state (AOS) of the sample was determined using a potentiometric titration method that has been described in detail elsewhere.<sup>13</sup>

*2.4. Thermal Analyses.* Thermogravimetric analyses (TGA) data were collected using a Hi-Res TGA 2950 model thermogravimetric analyzer. The experiments were carried out in a  $N_2$  or  $O_2$  atmosphere. The temperature ramp was 10 °C/min for each analysis. Temperature-programmed desorption–mass spectrometry (TPD-MS) experiments were performed using a furnace and a MKS-UTI PPT quadrupole residual MS gas analyzer. A-OMS-2 samples (~50 mg) were loaded into a quartz tube fixed in the furnace. After being purged with He for 6 h, the powder sample was heated at a rate of 10 °C/min to 700 °C. The evolved compounds were screened with a mass spectrometer.

*2.5.  $N_2$  Adsorption/Desorption and Pore Size Distribution.* The isothermal  $N_2$  adsorption/desorption experiments were conducted on a Micromeritics ASAP 2010 surface area and porosimetry system. The samples were pre-degassed at 200 °C for 15 h. Nitrogen gas was used as an adsorbate at liquid nitrogen temperature. Specific surface areas were calculated by the BET method. Pore size distribution was also measured.

**3. Catalytic Evaluation.** The aerobic oxidation of cyclohexanol to cyclohexanone was performed using a procedure described in detail elsewhere.<sup>9</sup> A-OMS-2 nanofibrous materials, except for H-OMS-2, were ground and dried at 110 °C overnight to eliminate the moisture. A solution of 1 mmol of cyclohexanol and 10 mL of toluene (solvent) was mixed with 50 mg of A-OMS-2 catalyst in a round-bottomed flask. At 110 °C, the mixture was stirred with refluxing with an airflow for 4 h. The reaction mixture was allowed to cool to room temperature. A-OMS-1 catalysts were removed by filtration. The filtrate was then analyzed using gas chromatography/mass spectrometry (GC/MS) to determine the selectivity and conversion.

## Results

**1. XRD and TEM Studies.** The phase and morphology transformation processes of the A-OL-1 materials to A-OMS-2 products have been studied using XRD and TEM. According to the XRD and TEM data, the phase and morphology transformation processes of thin film-like A-OL-1 materials to A-OMS-2 nanofibers were found to be similar to that of Mg-OMS-1 nanoribbons, which has been explained in a previous paper.<sup>26</sup>

X-ray diffraction patterns for Li-OMS-2, Na-OMS-2, K-OMS-2, and Rb-OMS-2 are shown in Figure 1. All of the peaks corresponded to the pure crystalline phase of cryptomelane ( $KMn_8O_{16}$ , JCPDS 29-1020). The relative intensity of the (110) peak is higher than that in the standard JCPDS data, which is due to the preferred orientation of nanofibrous structures. The nanofibrous materials tend to lie on their (110) planes, revealed by TEM data (see below). On the basis of the intensities and broadness of the major diffraction peaks, except (110) peaks, the crystallinities of the A-OMS-2 materials increase in the order Na-OMS-2 < Li-OMS-2 < K-OMS-2 < Rb-OMS-

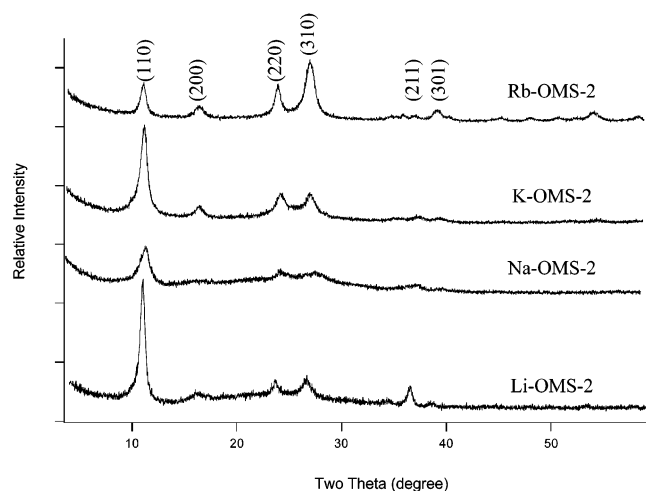


Figure 1. XRD patterns of Li-, Na-, K-, and Rb-OMS-2.

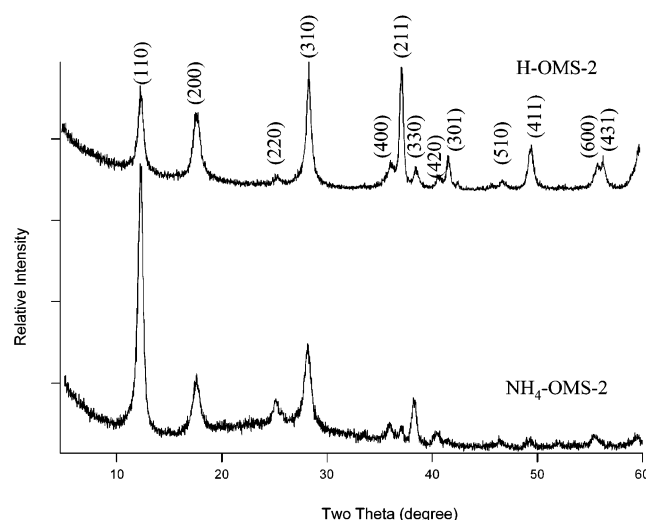


Figure 2. XRD patterns of  $\text{NH}_4\text{-OMS-2}$  and the calcination product H-OMS-2.

2. Figure 2 shows the XRD patterns of  $\text{NH}_4\text{-OMS-2}$  and the corresponding calcined product H-OMS-2 prepared at 380 °C for 7 h. Both  $\text{NH}_4\text{-}$  and H-OMS-2 were determined to have the cryptomelane structure. The crystallinity of  $\text{NH}_4\text{-OMS-2}$  was similar to that of K-OMS-2. In addition, the cryptomelane structure of H-OMS-2 was maintained after the calcination, and the crystallinity was improved from that of the  $\text{NH}_4\text{-OMS-2}$  precursor, as indicated by the increasing intensity of the XRD peaks and the presence of those less intense XRD peaks that were not observed in the  $\text{NH}_4\text{-OMS-2}$  pattern.

These XRD patterns of A-OMS-2 materials, shown in Figures 1 and 2, were the final products transformed from A-OL-1 precursors and were prepared at different temperatures for different periods of time in order to achieve complete transformation. The  $d$  spacing distances of (110) planes of each A-OMS were measured from XRD patterns and are listed in Table 1. The temperature and time of hydrothermal heating for the preparation of the A-OMS-2 materials have been investigated. The effects of the heating temperatures and times are presented in Figure 3. For Li-OMS-2, the transformation from Li-OL-1 to the cryptomelane materials was not complete at a temperature of 150 °C or lower. At 200 °C, the transformation to Li-OMS-2 was complete after 24 h. At a higher temperature (e.g., 240 °C), only 8 h was needed to complete the formation

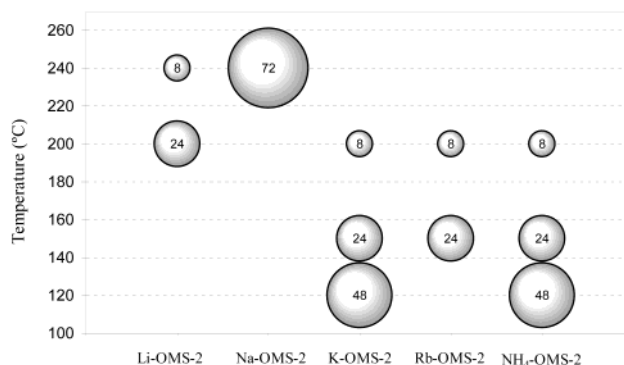


Figure 3. Effects of temperature and time of hydrothermal heating on the preparation of A-OMS-2 materials. The sizes of the bubbles represent the heating time to complete the transformation to A-OMS-2 materials. The values of the heating times (hours) are shown in the center of the bubbles.

TABLE 1:  $d$  Spacings of (110) Plans of A-OMS-2 Materials from XRD Diffraction Data and Unit Cell Parameters  $\beta$  from Electron Diffraction Data

sample	$d$ -spacing of (110) (Å)	$\beta$ (°)
H-OMS-2	6.735	91.5
Li-OMS-2	7.341	91.1
Na-OMS-2	6.964	90.9
K-OMS-2	7.105	90.5
$\text{NH}_4\text{-OMS-2}$	7.238	90.5
Rb-OMS-2	7.272	90.5

of Li-OMS-2. For Na-OMS-2, the transformation required the highest temperature and longest time. The final product of Na-OMS-2 was formed at 240 °C after 72 h. K-OMS-2 materials could be synthesized at a relatively low temperature, such as 120 °C, after heating for 48 h. The times of transformation to K-OMS-2 from K-OL-1 were shortened with increasing heating temperature. Rb-OMS-2 could not be formed at 120 °C. When the temperature was increased to 150 and 200 °C, the transformation from Rb-OL-1 to Rb-OMS-2 was complete after 24 and 8 h, respectively. For the syntheses of  $\text{NH}_4\text{-OMS-2}$ , the temperatures and heating time needed are similar to those for K-OMS-2.

Microstructures of these A-OMS-2 materials have been studied by TEM. TEM bright-field images of Li-OMS-2, K-OMS-2, Rb-OMS-2, and  $\text{NH}_4\text{-OMS-2}$  with the corresponding selected-area electron diffraction (SAED) patterns are shown in Figure 4. All of these materials are in the form of nanofibers, according to the TEM bright-field images. SAED experiments indicated that these nanofibrous materials preferred to lie on their (110) planes. Lattice fringes were clearly observed in all of the four A-OMS-2 materials. The tunnels are well ordered continuously along the  $c$  dimension. The distance between the lattice fringes are around 0.69 nm. The  $d$  spacings of (110) planes were measured from the SAED patterns.  $\text{NH}_4\text{-OMS-2}$ , Li-OMS-2, K-OMS-2, and Rb-OMS-2 materials have similar  $d$  spacing distance around 0.69 nm. However, the  $d$  spacing value measured by XRD was more accurate (Table 1). The unit cell parameters  $c$  and  $\beta$  were also measured from the SAED patterns for these materials. All of these three A-OMS-2 materials have similar values for  $c$  around 0.28 nm. The unit cell parameters  $\beta$  are listed in Table 1.

Due to the poor crystallinity of Na-OMS-2 materials, the lattice fringes were not as well formed as those of other A-OMS-2 materials, as revealed in Figure 5 which was taken using the JEOL 2010 Fas TEM. In some areas of the Na-OMS-2 materials, the growth of the tunnel is not continuous



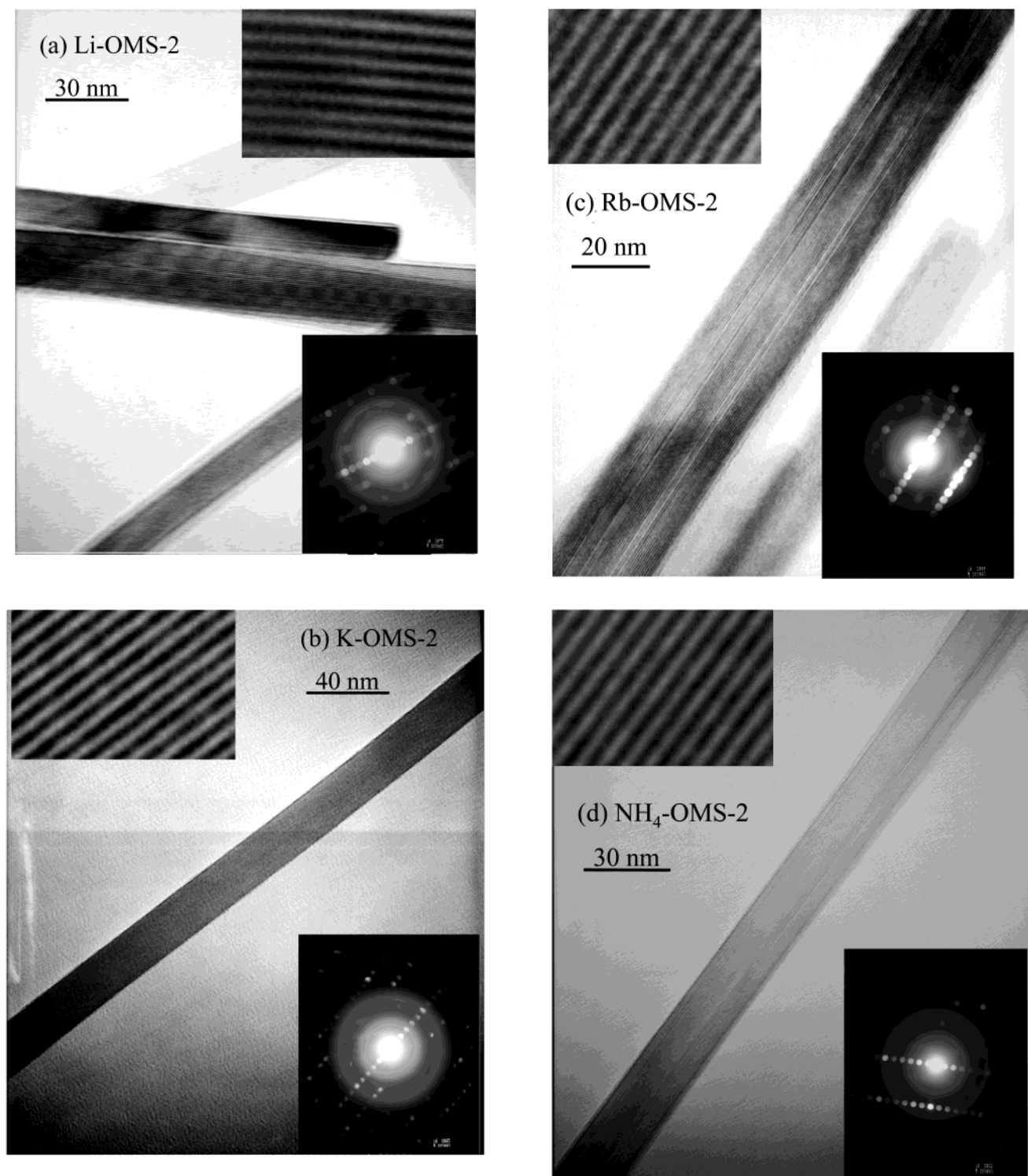


**Figure 4.** TEM bright-field images, the enlarged images of lattice fringes, and the corresponding selected-area diffraction patterns of nanofibers: (a) Li-OMS, (b) K-OMS-2, (c) Rb-OMS-2, (d)  $\text{NH}_4$ -OMS-2.

(Figure 5a). In other areas, the growth of the tunnel is not homogeneous and some disordered tunnel structures were observed (Figure 5b). The tunnel structures of different sizes were observed. Due to the poor crystallinity of the materials and the small amount of disorder, the other phase was unable to be observed in the XRD pattern of Na-OMS-2.

**2. Morphology.** The morphologies of A-OMS-2 materials are shown in Figure 6. Generally, A-OMS-2 materials have nanofibrous shapes with widths of a few tens of nanometers. The TEM tilting experiments showed that most of the fibers

had uniform diameters, which is different from that of nano-ribbonlike materials in the previous paper.<sup>26</sup> The lengths of these nanofibers vary from a few hundred nanometers to several tens of micrometers. The lengths of K- and Rb-OMS-2 nanofibers are the shortest, and  $\text{NH}_4$ - and H-OMS-2 nanofibers are the longest. Besides the nanofibrous morphologies, some nanoparticles were observed in each of the A-OMS-2 materials. Li-OMS-2 materials have the largest quantity of nanoparticles, and  $\text{NH}_4$ - and H-OMS-2 materials have the least quantity of nanoparticles.

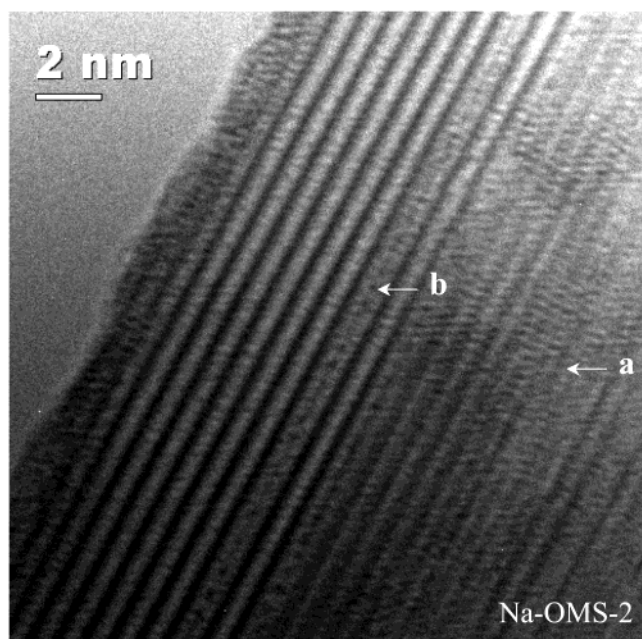


**Figure 5.** A HREM image of a Na-OMS-2 nanofiber. (a) Discontinuous growth of cryptomelane tunnel structure. (b) Disordered tunnel structures.

### 3. Chemical Compositions and Average Oxidation State.

To determine the absolute compositions of A-OMS-2 materials, ICP analyses were done. The results of the measured atomic ratio of alkali metal cations and manganese ions are listed in Table 2. The amount of ammonium and hydronium in  $\text{NH}_4$ -OMS-2 and H-OMS-2 materials were unable to be analyzed due to the determination limitation of the instrument. Elemental analysis data reveal the sequence for alkali cation atomic composition:  $\text{Li} > \text{K} > \text{Rb} > \text{Na}$ .

Average oxidation states (AOS) of manganese of all of six A-OMS-2 materials were determined using a potentiometric titration method. The results are also shown in Table 2. The average oxidation states range from 3.63 to 3.92 depending on the nature of the tunnel cations. The sequence of average oxidation states is  $\text{Li-OMS-2} < \text{K-OMS-2} < \text{Rb-OMS-2} < \text{Na-OMS-2} < \text{NH}_4\text{-OMS-2} < \text{H-OMS-2}$ . This AOS sequence in alkali cation OMS-2 materials is the opposite of that for the atomic compositions of cations in the materials. On the basis of the elemental analysis and AOS data, the formula of the four OMS-2 containing alkali cations were calculated and are listed in Table 2.

**4. Thermal Stability.** The thermal stabilities of A-OMS-2 materials were studied using TGA in a  $\text{N}_2$  atmosphere and TPD in a He atmosphere in the range of 30–700 °C. Both  $\text{N}_2$  and He are inert gases for OMS-2 materials. The TGA data for Li-, Na-, K-, Rb-, and  $\text{NH}_4$ -OMS-2 are shown in Figure 7. The oxygen and water evolutions of these A-OMS-2 materials revealed by TPD-MS are shown in Figures 8 and 9, respectively.

From the TGA data for Li-OMS-2 (Figure 7), it can be seen that the first weight loss (~4%) is in the range of 150–250 °C, which is due to the physically sorbed water. This water evolution peak is not shown in the TPD data (Figure 8) because all of the samples for TPD were pretreated with He for 6 h. The second TGA weight loss (~3%) of Li-OMS-2 is in the range of 300–400 °C, which is mainly due to evolution of the water chemically sorbed in the materials (Figure 9) and small amounts of active oxygen species in the materials corresponding to the first oxygen peak of Li-OMS-2 in Figure 8. The last TGA weight loss

(~2%) of Li-OMS-2 is in the range of 520–600 °C (Figure 7), corresponding to the second oxygen peak of Li-OMS-2 in Figure 8, which is due to evolution of the structural oxygen in the framework of the tunnels. According to the TGA and TPD data of Li-OMS-2, the thermal stability of Li-OMS-2 is about 550 °C in an inert atmosphere.

From TGA data for Na-OMS-2 materials (Figure 7), a large amount of weight loss (~12%) took place in the range of 30–200 °C. This weight loss corresponds to the large water evolution peak in the TPD data (Figure 9). The second weight loss (~10%) in the TGA data is in the range of 500–670 °C (Figure 7), which is due to the oxygen and water evolution from the materials (Figures 8 and 9). According to the TGA and TPD data for Na-OMS-2, the thermal stability of Na-OMS-2 is about 500 °C in an inert atmosphere.

For K- and Rb-OMS-2 materials, similar thermal behaviors were observed in both TGA and TPD data. Both of these two materials contain a very small amount of water, as revealed in the water evolution plots in Figure 9. The evolution of active oxygen species of these two materials was detected at about 500–700 °C (Figure 8), corresponding to the weight loss (~4%) starting from 600 °C in the TGA plots of these two materials (Figure 7). Framework oxygen loss was observed at about 700 °C in TPD (Figure 8). According to the TGA and TPD data for K- and Rb-OMS-2, the thermal stabilities are at least 700 °C in an inert atmosphere.

$\text{NH}_4$ -OMS-2 materials have more tunnel water than that in K- and Rb-OMS-2, according to the TPD data (Figure 9), which caused the large weight loss (~10%) of  $\text{NH}_4$ -OMS-2 materials in the range of 450–530 °C (Figure 7). The weight loss was also due to the oxygen evolution from the materials in a similar temperature range (Figure 8). The thermal stability of  $\text{NH}_4$ -OMS-2 materials, according to the TGA and TPD data, is about 450 °C in an inert atmosphere. The calcined products of  $\text{NH}_4$ -OMS-2 materials, H-OMS-2 materials, showed similar thermal behaviors in TGA and TPD experiments (data are not shown here.).

**5.  $\text{N}_2$  Adsorption/Desorption Isotherms and Pore Size Distribution.** The isotherm plots for  $\text{N}_2$  adsorption/desorption of A-OMS-2 materials and the pore size distribution profile using the H-K model of Rb-OMS-2 are shown in Figures 10A and 10B, respectively. Pore size distribution profiles of other A-OMS-2 materials were similar to the one of Rb-OMS-2, showing a PSD peak in the range of 4.8–5.6 Å, which revealed the existence of micropores. However, the micropore volumes of these A-OMS-2 materials were small compared to their total pore volumes (Table 3). The average pore diameters ranged from 157 to 249 Å, indicating a large amount of slit-shaped mesopores with nonuniform sizes or shapes in the materials.<sup>16,29</sup> The textural properties of A-OMS-2 materials are similar to those of the conventional bulk OMS-2 materials.<sup>16</sup> The isotherm plots (Figure 10A) show steep increases at a low relative pressure ( $P/P_0 < 0.01$ ), also suggesting the micropore filling of  $\text{N}_2$  atoms. BET surface areas of A-OMS-2 materials were measured and listed in Table 3. Na-OMS-2 has the highest surface area of all of the A-OMS-2 materials.

**6. Catalytic Evaluation.** The catalytic activities of A-OMS-2 materials were evaluated with the aerobic oxidation of cyclohexanol to cyclohexanone. The selectivity of A-OMS-2 in this reaction was measured to be 100%. The conversions are listed in Table 3. The highest conversion was achieved using Li-OMS-2. According to the data in Table 3, the catalytic conversions and surface areas of A-OMS-2 materials are related to each other. For most of the A-OMS-2 materials, when the



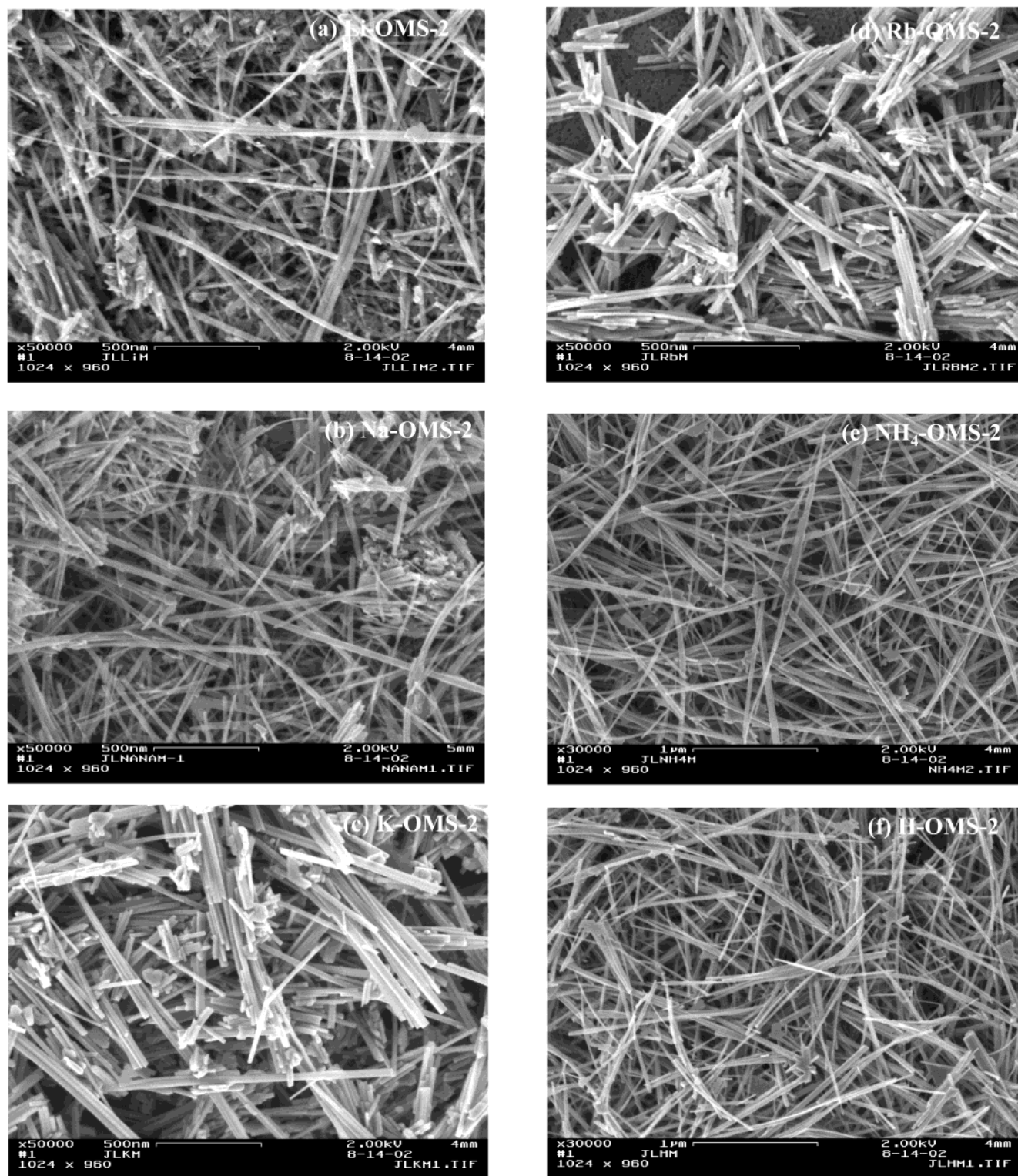


**Figure 6.** Secondary electron SEM images of the morphologies for A-OMS-2 materials: (a) Li-OMS-2; (b) Na-OMS-2; (c) K-OMS-2; (d) Rb-OMS-2; (e)  $\text{NH}_4$ -OMS-2; (f) H-OMS-2.

surface area of the catalyst was increased, the conversion for the reaction increased.

### Discussion

On the basis of the XRD and TEM data, the phase and morphology transformation of the thin film-like A-OL-1 to nanofiberlike A-OMS-2 are similar to those of thin film-like Mg-OL-1 to nanoribbonlike Mg-OMS-1.<sup>26</sup> Briefly, the nanofibers formed from the thin-film precursors at an early stage of

the hydrothermal heating, followed by the appearance of lattice fringes which indicated the formation of tunnel structures. The formation of tunnel resulted from some of the Mn(III) octahedra from the layers of the precursors migrating into the interlayer region and becoming corner-sharing octahedra that assist in the formation of the "walls" of the tunnels. The present paper will concentrate only on the effects of cation templates on the synthesis and properties of the A-OMS-2 materials.

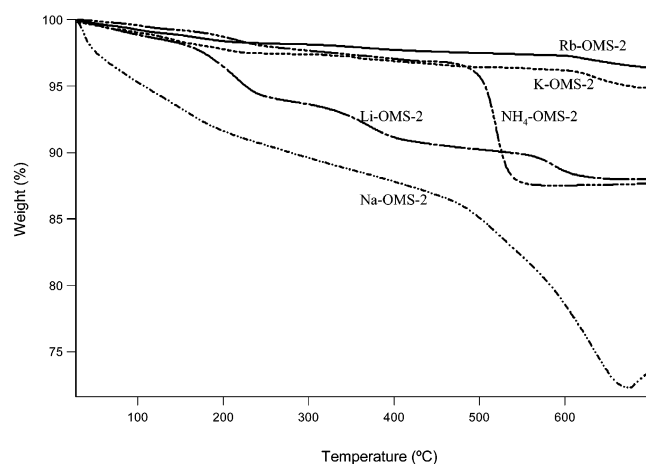


**Figure 7.** TGA plots for Li-, Na-, K-, Rb-, and NH<sub>4</sub>-OMS-2 materials in a N<sub>2</sub> atmosphere from 30 to 700 °C with a ramp of 10 °C/min.

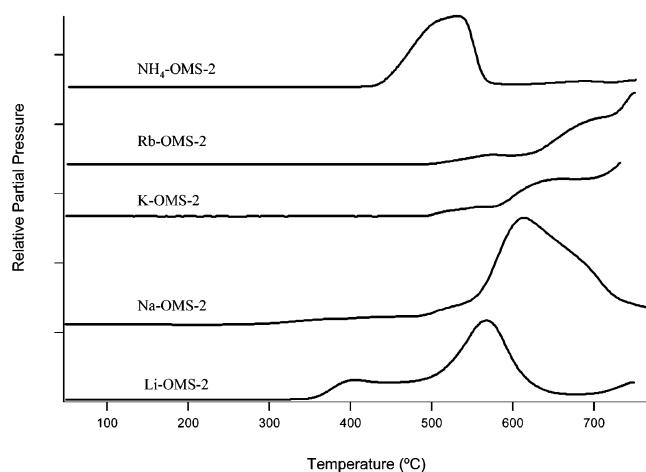


**Figure 8.** Oxygen evolution of Li-, Na-, K-, Rb-, and NH<sub>4</sub>-OMS-2 materials revealed by TPD-MS in a He atmosphere from 30 to 700 °C with a ramp of 10 °C/min.

**TABLE 2: Effects of Cation Sizes on the Elemental Compositions and Average Oxidation States of Mn in A-OMS-2 Materials**

sample	Shannon radius of the cation A <sup>+</sup> (Å) <sup>a</sup>	atomic ratio of A/Mn	average oxidation state of Mn	formula
Li-OMS-2	0.92	0.688	3.78	Li <sub>0.62</sub> Mn <sub>0.90</sub> O <sub>2</sub> •1.78H <sub>2</sub> O
Na-OMS-2	1.18	0.170	3.83	Na <sub>0.17</sub> MnO <sub>2</sub> •1.42H <sub>2</sub> O
K-OMS-2	1.51	0.548	3.70	K <sub>0.52</sub> Mn <sub>0.94</sub> O <sub>2</sub> •1.13H <sub>2</sub> O
Rb-OMS-2	1.61	0.412	3.82	Rb <sub>0.39</sub> Mn <sub>0.95</sub> O <sub>2</sub> •1.17H <sub>2</sub> O
NH <sub>4</sub> -OMS-2	N/A	N/A	3.87	N/A
H-OMS-2	N/A	N/A	3.92	N/A

<sup>a</sup> Ref 28.

**1. Effects of Cation Templates on Transformation and Structures of A-OMS-2 Materials.** The optimal temperatures and heating times for the A-OMS-2 materials from their A-OL-1 precursors were found to be affected by the cation templates, as indicated by the XRD study on the crystallization processes of A-OMS-2 materials (Figure 3). Considering only alkali cations, potassium cations can be used to form the 2 × 2 tunnel structures at a relatively low temperature (120 °C) compared to the temperatures for syntheses using the other three alkali cations. Rubidium cations required a higher temperature (150 °C) to form the tunnel structure compared to that for

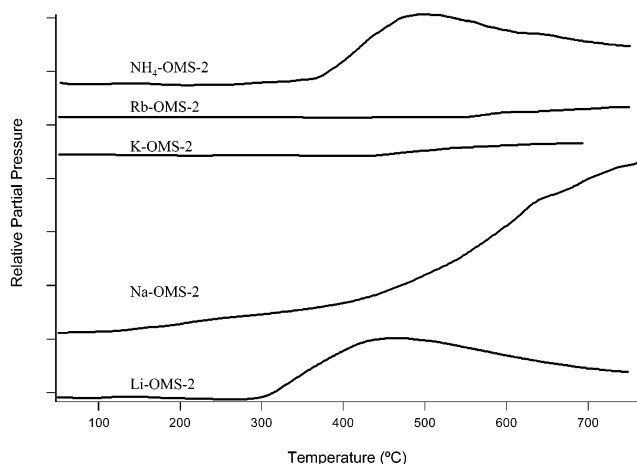


**Figure 9.** Water evolution in Li-, Na-, K-, Rb-OMS-2, and NH<sub>4</sub>-OMS-2 materials revealed by TPD-MS in a He atmosphere from 30 to 700 °C with a ramp of 10 °C/min.

**TABLE 3: Total Pore Volumes, Micropore Volumes, BET Surface Areas, and Catalytic Conversions in the Aerobic Oxidation of Cyclohexanol of A-OMS-2 Materials**

sample	total pore volume (cm <sup>3</sup> /g)	micropore volume (cm <sup>3</sup> /g)	BET surface area (m <sup>2</sup> /g)	conversion (%)
Li-OMS-2	0.4625	0.0049	76	23
Na-OMS-2	0.6772	0.0091	121	26
K-OMS-2	0.2269	0.0006	43	9
Rb-OMS-2	0.3244	0.0050	64	12
NH <sub>4</sub> -OMS-2	0.2359	0.0036	52	11
H-OMS-2	0.2207	0.0059	56	19

potassium cations. Lithium cations can form the tunnel structure at 200 °C after heating for 1 d. The condition to form the cryptomelane structures for sodium cations is the most critical compared to the other cations. Na-OMS-2 materials were formed at a temperature not lower than 240 °C with this synthetic method, and 3 days were needed to complete the synthesis. When using ammonium cations, the temperatures and heating times needed to form the tunnel structure are similar to those for potassium cations.

According to Fritsch et al.,<sup>31</sup> the effects of tunnel cations on the formation and structures of A-OMS-2 materials may be because the enthalpies of formation depend on the nature of cations and the amount of cations located in the tunnels. The enthalpy of the formation of 2 × 2 tunnel structure using large cations is lower than that of using small cations. The increasing content of tunnel cations in the materials can decrease the enthalpy of formation. Therefore, large cations (K<sup>+</sup>, NH<sub>4</sub><sup>+</sup>, and Rb<sup>+</sup>) decrease the enthalpy needed to form 2 × 2 tunnel structures compared with small cations (Li<sup>+</sup> and Na<sup>+</sup>). The less amount of sodium cations in the tunnels, compared with other alkali cations, increases the enthalpy of formation and makes Na-OMS-2 the most difficult one to synthesize among all of the A-OMS-2 materials.

The crystallinity and microstructures of A-OMS-2 materials were also affected by the tunnel cations, as indicated by the studies on crystallinity and microstructures (Figure 1, 2, 4, and 5). Although the use of rubidium cations did not lead to the formation of tunnel structures as easily as potassium cations, Rb-OMS-2 materials have the best crystallinity among all the alkali cations synthesized materials. K-OMS-2 materials have fairly good crystallinity compared to Na- and Li-OMS-2. The Na-OMS-2 materials have the least crystallinity. The small amount of disordered tunnel structures in Na-OMS-2 materials

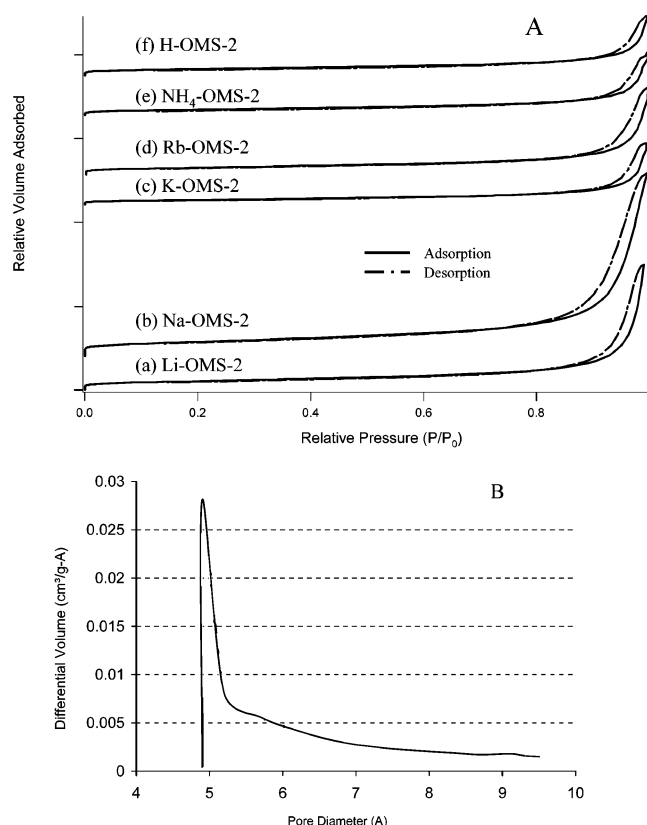


**Figure 10.** (A)  $\text{N}_2$  adsorption/desorption isothermal plots of Li-, Na-, K-, Rb-,  $\text{NH}_4$ -OMS-2, and H-OMS-2 materials. (B) The pore size distribution (PSD) plot measured with  $\text{N}_2$  using H-K slit pore model.

(Figure 5b) could be due to the intergrowth of other sizes of tunnels.<sup>30</sup>

According to Post et al.,<sup>1</sup> metal ions, such as potassium cations, are able to satisfy their ionic contact distances to the near oxygen atoms by occupying the special position (000) in the unit cell of cryptomelane, and the tunnels are not distorted. Therefore, these cations perfectly support the tunnel structures and stabilize the structure. Other metal ions, such as sodium cations, are smaller and thus form shorter cation-oxygen contacts. These smaller cations are displaced from the special position (000) in the tunnel and cause the tunnel distortion. Post et al.<sup>1</sup> also suggested that the symmetry of the unit cells could be lowered from tetragonal to monoclinic when the ratio of the radius of the manganese cations to that of the tunnel cations is greater than a certain value.

In the structures of A-OMS-2 materials, the lithium and sodium cations probably are displaced from the center of the tunnels in the structures and the crystal structures are distorted and changed to monoclinic symmetry, indicated by the increasing value of the unit cell parameter  $\beta$ , because the sizes of lithium and sodium cations are small (Table 2). The large cations, such as potassium, rubidium, and ammonium cations can occupy the special positions in the tunnels and preserve the symmetry of the structure, evidenced by the unit cell parameter  $\beta$  being very close to  $90^\circ$ . This probably is the reason that  $\text{NH}_4$ -, K- and Rb-OMS-2 materials have more ordered tunnel structures than Li- and Na-OMS-2 materials do, as well as request lower temperatures or shorter heating times to prepare.

Thackeray et al. reported ammonium manganese oxide materials with cryptomelane-type structures which were prepared using  $\alpha\text{-MnO}_2$  powder precursor at a firing temperature in an  $\text{NH}_3/\text{Ar}$  atmosphere.<sup>32</sup> The ammonium manganese oxide

materials were handled in a moisture-free environment. Therefore, the water content in the ammonium manganese oxide materials was very low. The materials had tetragonal structures. The  $\text{NH}_4$ -OMS-2 materials prepared in this research have lower symmetry, compared with the structure of the materials prepared by Thackeray et al., and have pseudo-tetragonal structures. This is probably due to more water content in the tunnels in  $\text{NH}_4$ -OMS-2 materials, which resulted from the hydrothermal synthesis.

Sodium cations should have led to a better structural symmetry than lithium cations. However, the existence of a large amount of tunnel water molecules, revealed from the TPD data (Figure 9), may cause more disorder in the structure of Na-OMS-2 materials as well as the critical synthetic condition to form the tunnel structure using sodium cation templates.

The nature and amount of the cation templates and the amount of water molecules in the tunnel also affected the tunnel sizes of some A-OMS-2 materials. For example, Li-OMS-2 had a larger tunnel than Na-OMS-2, indicated by the  $d$  spacings of (110) planes of these two materials (Table 1). This is due to Li-OMS-2 had more cations and water molecules in the tunnels than Na-OMS-2, as evidenced by elemental compositions in Table 2. For K-OMS-2 and Rb-OMS-2, the Shannon radius of  $\text{Rb}^+$  is larger than that of  $\text{K}^+$  and more water molecules reside in Rb-OMS-2, indicated by the data in Table 2. However, the tunnel size of Rb-OMS-2 is only slightly larger than that of K-OMS-2 because less  $\text{Rb}^+$  cations reside in the tunnels (Table 2).

## 2. Effects of Cation Templates on the Chemical and Physical Properties of A-OMS-2 Materials.

The difference in the cation templates also affects the chemical and physical properties of A-OMS-2 materials, such as the thermal stability, chemical composition, and average oxidation state of manganese. In the natural or synthetic bulk cryptomelane materials, the tunnel sites are not fully occupied by tunnel cations.<sup>1,2</sup> Water molecules fill some of the tunnel sites that are not occupied by the cations. Some of the octahedral sites of manganese are also vacant.<sup>33</sup> For K- and Rb-OMS-2 materials, there are very small amounts of water absorbed in the materials, as indicated by TGA and TPD data (Figure 9). The tunnel sites probably are occupied with potassium or rubidium cations more than they are in the Li- and Na-OMS-2. These two materials are more hydrophobic than Li- and Na-OMS-2 materials. The atomic ratios of potassium and rubidium cations to manganese cations in each A-OMS-2 material are relatively larger than the ideal ratio of K/Mn (0.25) in cryptomelane,<sup>11,12</sup> which may indicate more vacancies in octahedral sites of manganese. Li-OMS-2 materials have more chemically sorbed water than in K- and Rb-OMS-2 (Figure 9). Na-OMS-2 materials contain a lot of water. These water molecules may occupy more of the tunnel cation sites, which results in less sodium cations in the Na-OMS-2 materials, revealed by a smaller value of the atomic ratio of Na/Mn (0.170) than that in other OMS-2 materials. Na-OMS-2 materials are less hydrophobic than the other three alkali-cation synthesized OMS-2 materials.

For alkali-cation synthesized OMS-2 materials, the thermal stabilities are related to the cation sizes. The sequence of the thermal stabilities of alkali cation-OMS-2 materials is Li-OMS-2 < Na-OMS-2 < K-OMS-2 < Rb-OMS-2. This is probably due to the larger cations leading to higher structural symmetry and a more stable structure. Therefore, the larger the cations are, the greater the thermal stability of the materials is. The size of ammonium cations is similar to that of potassium cations. The thermal stability of  $\text{NH}_4$ -OMS-2 materials should



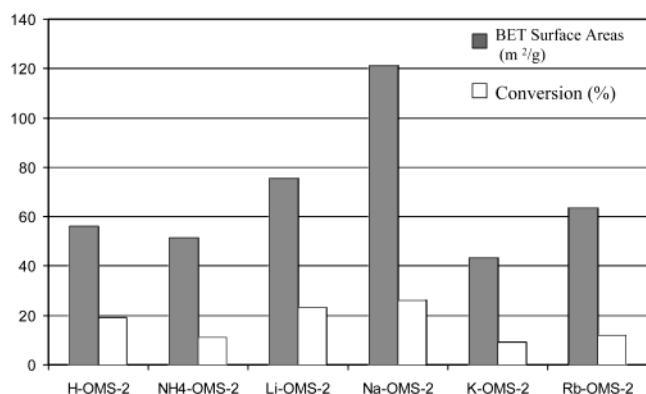


**Figure 11.** The relationship between the surface areas of A-OMS-2 materials and their catalytic conversions on the aerobic oxidation of cyclohexanol to cyclohexanone.

have been similar to that of K-OMS-2 since their tunnel cations have similar sizes. However, NH<sub>4</sub>-OMS-2 materials have more tunnel water than K-OMS-2 materials, which causes lower thermal stability of NH<sub>4</sub>-OMS-2 than K-OMS-2 materials. The formation of tunnel H<sup>+</sup> cations during the heating of NH<sub>4</sub>-OMS-2 may also produce lower thermal stability of NH<sub>4</sub>-OMS-2 than K-OMS-2 because the small H<sup>+</sup> cations cannot support the tunnel as well as large cations such as potassium.

**3. The Relationship between Surface Areas and the Catalytic Activities of the A-OMS-2 Materials.** The catalytic activities of A-OMS-2 materials are related to the physical and chemical properties of the materials, such as surface areas and average oxidation states of manganese.<sup>4,5</sup> In the aerobic oxidation of cyclohexanol using A-OMS-2 materials as catalysts, the conversions in the reaction were found to be related to the surface areas of the materials (Figure 11). The higher the surface area is, the more catalytic active sites the catalyst has, and the better the catalytic performance is. The surface area is not the only factor influencing the catalytic activity of A-OMS-2 catalysts. Average oxidation states of manganese also play a key role in the catalytic activity. For example, the surface area of Rb-OMS-2 is higher than that of H-OMS-2, but the conversion of Rb-OMS-2 is lower than that of H-OMS-2, which may be due to the higher AOS in H-OMS-2 than that in Rb-OMS-2. We have previously observed that optimization of CO oxidation catalysts, such as Cu-OMS-2, Co-OMS-2, and Ag-OMS-2, are also related to manganese AOS that are high (approaching 4.0) but contain some reduced Mn(IV).<sup>7</sup>

## Conclusions

Cryptomelane-type materials have been successfully synthesized using four alkali metal cations (Li<sup>+</sup>, Na<sup>+</sup>, K<sup>+</sup>, and Rb<sup>+</sup>) and ammonium cations (NH<sub>4</sub><sup>+</sup>). These nanofibrous materials are transformed from their thin-film-like layered structure manganese oxide (A-OL-1) precursors. Li- and Rb-OMS-2 have been synthesized for the first time. H-OMS-2 materials were prepared by calcining NH<sub>4</sub>-OMS-2 at 380 °C. All of the A-OMS-2 materials have nanofibrous morphologies with various widths on the order of nanometers and various lengths on the order of micrometers. Transmission electron microscopy bright field images and electron diffraction patterns show that the nanofibrous crystals of Li-, K-, Rb-, and NH<sub>4</sub>-OMS-2 have uniform lattice fringes, which indicate long-range order in the form of 2 × 2 tunnels along the *b* axis. Na-OMS-2

nanofibrous materials have disordered tunnel structures in some areas. Crystallinity and microstructures largely depend on the size of the cations and the amount of tunnel water. The larger cations lead to better crystallinity and a more ordered tunnel structure, while more tunnel water decreases the order in the tunnel structure. Thermal stabilities of the materials also are affected by the nature of the cations and the amount of water in the materials. Larger cations lead to higher thermal stability, while more tunnel water decreases the stability of the tunnel structure at high temperature (>550 °C). The catalytic activities of the A-OMS-2 materials are related to the surface areas. Higher surface areas lead to better catalytic performance of the materials in most materials.

**Acknowledgment.** We acknowledge support by the Geosciences and Biosciences Division, Office of Basic Energy Sciences, Office of Science, U.S. Department of Energy. We also thank Dr. Francis S. Galasso for helpful discussions.

## References and Notes

- (1) Post, J. E.; Von Dreele, R. B.; Buseck, P. R. *Acta Crystallogr.* **1982**, B38, 1056–1065.
- (2) Post, J. E.; Burnham, C. W. *Am. Mineral.* **1986**, 71, 1178–1185.
- (3) Tsuji, M.; Abe, M. *Solvent Extr. Ion Exch.* **1984**, 2, 253–274.
- (4) Suib, S. L.; Iton, L. E. *Chem. Mater.* **1994**, 6, 429–433.
- (5) Suib, S. L. *Curr. Opin. Solid State Mater. Sci.* **1998**, 3, 63–70.
- (6) Brock, S. L.; Duan, N.; Tian, Z. R.; Giraldo, O.; Zhou, H.; Suib, S. L. *Chem. Mater.* **1998**, 10, 2619–2628.
- (7) Xia, G. G.; Yin, Y. G.; Willis, W. S.; Wang, J. Y.; Suib, S. L. *J. Catal.* **1999**, 185, 91–105.
- (8) Chen, X.; She, Y.-F.; Suib, S. L.; O'Young, C. L. *J. Catal.* **2001**, 197, 292–302.
- (9) Son, Y.-C.; Makwana, V. D.; Howell, A. R.; Suib, S. L. *Angew. Chem., Int. Ed.* **2001**, 40, 4280–4283. (b) Makwana, V. D.; Son, Y.-C.; Howell, A. R.; Suib, S. L. *J. Catal.* **2002**, 210, 46–52.
- (10) Giovanoli, R.; Balmer, B. *Chimia* **1981**, 35, 53–55. (b) Giovanoli, R.; Faller, M. *Chimia* **1989**, 43, 54–56.
- (11) Golden, D. C.; Dixon, J. B.; Chen, C. C. *Clays Clay Miner.* **1986**, 34, 511–520.
- (12) Golden, D. X.; Chen, C. C.; Dixon, J. B. *Clays Clay Miner.* **1987**, 35, 271–280.
- (13) Cai, J.; Liu, J.; Willis, W. S.; Suib, S. L. *Chem. Mater.* **2001**, 13, 2413–2422.
- (14) Strobel, P.; Charenton, J. C. *Rev. Chim. Miner.* **1986**, 23, 125–137.
- (15) De Guzman, R. N.; Shen, Y.-F.; Shaw, B. R.; Suib, S. L.; O'Young, C.-L. *Chem. Mater.* **1993**, 5, 1395–1400. (b) De Guzman, R. N.; Shen, Y.-F.; Neth, E. J.; Suib, S. L.; O'Young, C.-L.; Levine, S.; Newsam, M. *Chem. Mater.* **1994**, 6, 815–821. (c) De Guzman, R. N. M.S. Thesis, The University of Connecticut, 1994.
- (16) Chen, X.; Shen, Y.-F.; Suib, S. L.; O'Young, C. L. *Chem. Mater.* **2002**, 12, 940–948.
- (17) Luo, J.; Zhang, Q.; Huang, A.; Suib, S. L. *Microporous Mesoporous Mater.* **2000**, 35–36, 209–217.
- (18) Feng, Q.; Kanoh, H.; Miyai, Y.; Ooi, K. *Chem. Mater.* **1995**, 7, 148–153.
- (19) Ching, S.; Roark, J. L.; Duan, N.; Suib, S. L. *Chem. Mater.* **1997**, 9, 750–754.
- (20) Duan, N.; Suib, S. L.; O'Young, C. L. *J. Chem. Soc., Chem. Commun.* **1995**, 13, 1367–1368.
- (21) O'Young, C. L. In *Synthesis of Microporous Materials*; Occelli, M. L.; Robson, H. E., Eds.; Van Nostrand Reinhold: Washington, DC, 1992; pp 333–340.
- (22) Feng, Q.; Yanagisawa, K.; Yamasaki, N. *J. Porous Mater.* **1998**, 5, 153–161. (b) Feng, Q.; Horiuchi, T.; Mitsusio, T.; Yanagisawa, K.; Yamasaki, N. *J. Mater. Sci. Lett.* **1999**, 18, 1375–1378.
- (23) Feng, Q.; Kanoh, H.; Ooi, K. *J. Mater. Chem.* **1999**, 9, 319–333.
- (24) Baghurst, D. R.; Mingos, D. M. P. *J. Chem. Soc., Chem. Commun.* **1988**, 12, 829–830.
- (25) Tong, W. Ph.D. Thesis, The University of Connecticut, 2002.
- (26) Liu, J.; Cai, J.; Son, Y.-C.; Gao, Q.; Suib, S. L.; Aindow, M. *J. Phys. Chem. B* **2002**, 106, 9761–9768.
- (27) Brock, S. L.; Sanabria, M.; Suib, S. L. *J. Phys. Chem. B* **1999**, 103, 7416–7428. (b) Brock, S. L.; Sanabria, M.; Nair, J.; Suib, S. L.; Ressler, T. J. *Phys. Chem. B* **2001**, 105, 5404–5410.
- (28) Shannon, R. D. *Acta Cryst.* **1976**, A32, 751–767.

(29) de Boer, J. H. In *The Structure and Properties of Porous Materials*; Everett, D. H., Stone, F. S., Eds.; Butterworth: London, 1958; p 68.

(30) Xia, G. G.; Tong, W.; Tolentino, E. N.; Duan, N.; Brock, S. L.; Wang, J.-Y.; Suib, S. L. *Chem. Mater.* **2001**, *13*, 1585–1592.

(31) Fritsch, S.; Post, J. E.; Suib, S. L.; Navrotsky, A. *Chem. Mater.* **1998**, *10*, 474–479.

(32) Johnson, C. S.; Dees, D. W.; Mansuetto, M. F.; Thackeray, M. M.; Vissers, D. R.; Argyriou, D.; Loong, C.-K.; Christensen, L. *J. Power Sources* **1997**, *68*, 570–577.

(33) Drits, V. A.; Silvester, E.; Gorshkov, A. I.; Manceau, A. *Am. Mineral.* **1997**, *82*, 946–961. (b) Silvester, E.; Manceau, A.; Drits, V. A. *Am. Mineral.* **1997**, *82*, 962–978.